

GAMOW-TELLER (GT_{\pm}) STRENGTH DISTRIBUTIONS OF ^{56}Ni FOR GROUND AND EXCITED STATES

Jameel-Un Nabi¹, Muneeb-Ur Rahman, Muhammad Sajjad

Faculty of Engineering Sciences, Ghulam Ishaq Khan Institute of Engineering
Sciences and Technology, Topi 23640, Swabi, NWFP, Pakistan

Gamow-Teller (GT) transitions play an important and consequential role in many astrophysical phenomena. These include, but are not limited to, electron and positron capture rates which determine the fate of massive stars and play an intricate role in the dynamics of core collapse. These GT_{\pm} transitions rates are the significant inputs in the description of supernova explosions. GT_{\pm} strength function values are sensitive to the ^{56}Ni core excitation in the middle pf -shell region and to the size of the model space as well. We used the pn-QRPA theory for extracting the GT strength for ground and excited states of ^{56}Ni . We then used these GT strength distributions to calculate the electron and positron capture rates which show differences with the earlier calculations. One curious finding of this paper is our enhanced electron capture rates on ^{56}Ni at presupernova temperatures. These differences need to be taken into account for the modeling of the early stages of Type II supernova evolution.

PACS numbers: 26.50.+x, 23.40.Bw, 23.40.-s, 21.60Jz

1. Introduction

Weak interactions play a conclusive role in the evolution of massive stars at the presupernova stage and supernova explosions. These explosions mark the end of the life of massive stars. The massive stars consist of concentric shells which are the relics of their previous burning phases. The helium burning shell continues to add ashes to the carbon-oxygen core. This results in the contraction of the core and eventually initiates the carbon burning which then leads to a variety of by-products, such as $^{16}_8\text{O}$, $^{20}_{10}\text{Ne}$, $^{23}_{11}\text{Na}$, $^{23}_{12}\text{Mg}$, and $^{24}_{12}\text{Mg}$ [1]. What follows is a succession of nuclear reaction sequences which depend sensitively on the mass of the star. When each reaction sequence reaches equilibrium, an “onion-like” shell structure develops in the interior of the star.

Stars with initial mass about $10M_{\odot}$ or more ignite carbon in the core non-degenerately [2]. Owing to neutrino (and antineutrino) emission at the high temperatures involved, due to e^{\pm} annihilation and other processes, subsequent evolution is greatly accelerated. The nuclear time-scale becomes shorter than the thermal one because carbon, oxygen, and silicon burning produce nuclei with masses progressively nearer the iron peak of the binding energy curve, and consequently less and less energy is generated per gram of fuel.

When the core attains high density and temperature, the photons having enough energy destroy heavy nuclei; a process known as photodisintegration. In a very short span, this photodisintegration reverses what the star has been

trying to do its entire life, i.e. to produce more massive elements than hydrogen and helium. This stripping down of iron to individual protons and neutrons is highly endothermic. This saps the thermal energy from the gas that would otherwise have resulted in the pressure necessary to support the core of the star.

At high temperature and density, the electrons supporting the star through degeneracy pressure are eaten up by heavy nuclei and protons that were produced during photodisintegration process, and thus lead to the neutronization of star. Electron capture and photodisintegration cost the core energy, reduce its electron density and this results in an accelerated core collapse. The collapse is very sensitive to entropy and to the number of lepton to baryon ratio, Y_e . These two quantities are mainly determined by weak interaction processes. In the inner region of the core, this collapse is homologous and subsonic having velocity of the collapse proportional to the distance away from the center of the star, while the outer regions collapse supersonically [3].

The structure of the progenitor star, including that of its core, plays a pivotal role in the development of the explosion process. Electron capture reduces the number of electrons available for pressure support. At higher densities, $\rho \approx 10^{11} g/cm^3$, electron capture produces neutrinos which escape the star carrying away energy and entropy from the core. Electron capture during the final evolution of a massive star is dominated by Fermi and Gamow-Teller (GT) transitions. The energies of the electrons are high enough to induce transitions to the GT resonance. The electron capture rates are very sensitive to the distribution of the GT_+ strength (in this direction a proton is changed into a neutron).

Bethe et al. [4] showed that, as a result of electron capture, the average number of nucleons per nucleus (\bar{A}) moves upward. Nevertheless, we can say that there is tendency for \bar{A} to increase with decreasing Y_e . During collapse, the entropy of the core decides whether electron capture occur on heavy nuclei or on free proton (produced during photodisintegration). The total entropy of the stellar core is the sum of the entropies due to nuclear excitation and that of the free nucleons. At low entropies ($S/k_B \approx 1$) captures on heavy nuclei dominate the total rate. These entropies of the stellar core do occur for the star of main sequence mass between 10 and 25 M_\odot and density range 10^9 - $10^{12} g/cm^3$ [5].

Electron captures on proton and positron captures on neutron play a very crucial role in the supernovae dynamics. During the collapse and accretion phases, these processes exhaust electrons, thus decreasing the degenerate pressure of electrons in the stellar core. Meanwhile, they produce neutrinos which carry the binding energy away. Therefore, electron and positron captures play key role in the dynamics of the formation of bounce shock of supernova. The Type II supernovae take place in heavy stars. The positron captures are of great importance in high temperature and low density locations. In such conditions, a rather high concentration of positron can be reached from $e^- + e^+ \leftrightarrow \gamma + \gamma$ equilibrium favoring the e^-e^+ pairs. The electron captures on proton and positron captures on neutron are considered important ingredients in the modeling of Type II supernovae [6].

Proton-neutron quasi particle random phase approximation (pn-QRPA) theory and shell model are extensively used for the calculations of capture rates in

the stellar environment. Each model has its own associated pros and cons. Shell model lays more emphasis on interaction of nucleons as compared to correlations whereas pn-QRPA puts more weight on correlations. One big advantage of using pn-QRPA theory is that it gives us the liberty of performing calculations in a luxurious model space (up to $7\hbar\omega$). The pn-QRPA method considers the residual correlations among the nucleons via one particle one hole (1p-1h) excitations in a large model spaces. The authors in [7] extended the QRPA model to configurations more complex than (1p-1h). The pn-QRPA formalism was successfully employed to calculate weak interaction rates for 178 sd-shell [7] and 650 fp/fpg-shell [8] nuclide in stellar matter. Later the decay and capture rates of nuclei of astrophysical importance were studied separately in detail and were compared with earlier calculations wherever possible both in sd-shell [9] and fp-shell (e.g. [10, 11]) regions.

Knowing the importance of the electron and positron capture processes in the evolution of stars many authors estimated these rates independently employing different models. Fuller et al. (referred as FFN) [12] estimated these rates for the nuclei in the mass range $A = 45 - 60$. They related these capture processes to the GT resonance. Aufderheide et al. [13, 14] then updated the rates of FFN and compiled a list of important nuclide and showed that these nuclide strongly affect Y_e via the electron capture processes. They ranked ^{56}Ni amongst the top ten nuclei which play a vital role in the deleptonization of the core. This isotope of nickel is abundant in the presupernova environment, and is considered to be a dominant role player among other iron-regime nuclei in the evolution of stellar core. The GT response is astrophysically important for a number of nuclide, particularly ^{56}Ni .

Recently the calculations of electron capture rates on ^{55}Co and ^{56}Ni using the pn-QRPA theory were presented and compared with earlier calculations [15]. There the authors also discussed the possible applications of these calculated rates in astrophysical environments. In this paper we present for the first time the GT strength distributions (both plus and minus) from the parent *and* excited states of ^{56}Ni . We also present the associated electron and positron capture rates for this important isotope of nickel. Comparison with earlier calculations wherever possible is also being presented. We used the pn-QRPA model to generate GT strength distributions and performed state by state calculations of the associated electron and positron capture rates. These calculated rates were summed over all parent and daughter states until satisfactory convergence was achieved.

We made the following assumptions to calculate electron and positron capture rates on ^{56}Ni .

1. Forbidden transitions were not taken into account. Only the allowed Gamow-Teller and superallowed Fermi transitions were calculated.
2. Electrons and positrons, in stellar matter, were assumed to follow the energy distribution of a Fermi gas.
3. Fermi functions were used in the phase space integrals to represent the dis-

tortion of electron (positron) wavefunctions (due to coulombic interactions of these with the nucleus).

4. Neutrinos and antineutrinos which are produced were assumed to escape freely from the core without interacting with any particle. We neglected the capture of (anti) neutrinos in our calculations.

2. General Formalism

In this paper we present the calculated capture rates on ^{56}Ni for the following two processes mediated by charge weak interaction:

1. Electron capture

$${}^A_Z X + e^- \rightarrow {}^A_{Z-1} X + \nu.$$

2. Positron capture

$${}^A_Z X + e^+ \rightarrow {}^A_{Z+1} X + \bar{\nu}.$$

These processes play an important role in the evolution of presupernova core. To calculate these electron capture and positron capture rates in the stellar environment, we used the following formalism.

The Hamiltonian of our model was chosen as

$$H^{\text{QRPA}} = H^{\text{sp}} + V^{\text{pair}} + V_{\text{GT}}^{\text{ph}} + V_{\text{GT}}^{\text{pp}}. \quad (1)$$

Here H^{sp} is the single-particle Hamiltonian, V^{pair} is the pairing force, $V_{\text{GT}}^{\text{ph}}$ is the particle-hole (ph) Gamow-Teller force, and $V_{\text{GT}}^{\text{pp}}$ is the particle-particle (pp) Gamow-Teller force. Wave functions and single particle energies were calculated in the Nilsson model [16], which takes into account the nuclear deformations. Pairing was treated in the BCS approximation. The proton-neutron residual interactions occur in two different forms, namely as particle-hole and particle-particle interaction. The interactions were given separable form and were characterized by two interaction constants χ (characterizing the particle-hole force) and κ (characterizing the particle-particle force). The selections of these two constants were done in an optimal fashion. For details of the fine tuning of the Gamow-Teller strength parameters, we refer to [17, 18]. In this work, we took the values of $\chi = 0.5 \text{ MeV}$ and $\kappa = 0.065 \text{ MeV}$ for ^{56}Ni .

Other parameters required for the calculation of capture rates are the Nilsson potential parameters, the deformation, the pairing gaps, and the Q-value of the reaction. Nilsson-potential parameters were taken from [19] and the Nilsson oscillator constant was chosen as $\hbar\omega = 41A^{-1/3}(\text{MeV})$, the same for protons and neutrons. The calculated half-lives depend only weakly on the values of the pairing gaps [20]. Thus, the traditional choice of $\Delta_p = \Delta_n = 12/\sqrt{A}(\text{MeV})$ was applied in the present work. For details regarding the QRPA wave functions

and calculation of weak rates we refer to [11]. Q-values were taken from the recent mass compilation of Audi et al. [21].

The Fermi operator is independent of space and spin, and as a result the Fermi strength is concentrated in a very narrow resonance centered around the isobaric analogue state (IAS) for the ground and excited states. The energy of the IAS was calculated according to the prescription given in [22, pp.111-112], whereas the reduced transition probability is given by

$$B(F) = T(T + 1) - T_{zi}T_{zf},$$

where T is the nuclear isospin, and T_{zi} , T_{zf} are the third components of the isospin of initial and final analogue states, respectively.

The parent excited states can be constructed as phonon-correlated multi-quasiparticles states. The transition amplitudes between the multi-quasiparticle states can be reduced to those of single-particle states. Excited states of an even-even nucleus are two-proton quasiparticle states and two-neutron quasiparticle states. Transitions from these initial states are possible to final proton-neutron quasiparticles pair states in the odd-odd daughter nucleus. The transition amplitudes and their reduction to correlated (c) one-quasiparticle states are given by

$$\langle p^f n_c^f | t_{\pm\sigma-\mu} | p_1^i p_{2c}^i \rangle = -\delta(p^f, p_2^i) \langle n_c^f | t_{\pm\sigma-\mu} | p_{1c}^i \rangle + \delta(p^f, p_1^i) \langle n_c^f | t_{\pm\sigma-\mu} | p_{2c}^i \rangle. \quad (2)$$

$$\langle p^f n_c^f | t_{\pm\sigma\mu} | n_1^i n_{2c}^i \rangle = +\delta(n^f, n_2^i) \langle p_c^f | t_{\pm\sigma\mu} | n_{1c}^i \rangle - \delta(n^f, n_1^i) \langle p_c^f | t_{\pm\sigma\mu} | n_{2c}^i \rangle. \quad (3)$$

Here $\mu = -1, 0, 1$, are the spherical components of the spin operator.

States in an odd-odd nucleus are expressed in quasiparticle transformation by two-quasiparticle states (proton-neutron pair states) or by four-quasiparticle states (three-proton, one-neutron or one-proton three-neutron quasiparticle states). The reduction of two-quasiparticle states to correlated (c) one-quasiparticle states is given by

$$\langle p_1^f p_{2c}^f | t_{\pm\sigma\mu} | p^i n_c^i \rangle = \delta(p_1^f, p^i) \langle p_{2c}^f | t_{\pm\sigma\mu} | n_c^i \rangle - \delta(p_2^f, p^i) \langle p_{1c}^f | t_{\pm\sigma\mu} | n_c^i \rangle. \quad (4)$$

$$\langle n_1^f n_{2c}^f | t_{\pm\sigma-\mu} | p^i n_c^i \rangle = \delta(n_2^f, n^i) \langle n_{1c}^f | t_{\pm\sigma-\mu} | p_c^i \rangle - \delta(n_1^f, n^i) \langle n_{2c}^f | t_{\pm\sigma-\mu} | p_c^i \rangle. \quad (5)$$

While four-quasiparticle states are simplified as

$$\begin{aligned} \langle p_1^f p_2^f n_1^f n_{2c}^f | t_{\pm\sigma-\mu} | p_1^i p_2^i p_3^i n_{1c}^i \rangle = & \delta(n_2^f, n_1^i) \left[\delta(p_1^f, p_2^i) \delta(p_2^f, p_3^i) \langle n_{1c}^f | t_{\pm\sigma-\mu} | p_{1c}^i \rangle \right. \\ & - \delta(p_1^f, p_1^i) \delta(p_2^f, p_3^i) \langle n_{1c}^f | t_{\pm\sigma-\mu} | p_{2c}^i \rangle \\ & + \delta(p_1^f, p_1^i) \delta(p_2^f, p_2^i) \langle n_{1c}^f | t_{\pm\sigma-\mu} | p_{3c}^i \rangle \Big] \\ & - \delta(n_1^f, n_1^i) \left[\delta(p_1^f, p_2^i) \delta(p_2^f, p_3^i) \langle n_{2c}^f | t_{\pm\sigma-\mu} | p_{1c}^i \rangle \right. \\ & - \delta(p_1^f, p_1^i) \delta(p_2^f, p_3^i) \langle n_{2c}^f | t_{\pm\sigma-\mu} | p_{2c}^i \rangle \\ & + \delta(p_1^f, p_1^i) \delta(p_2^f, p_2^i) \langle n_{2c}^f | t_{\pm\sigma-\mu} | p_{3c}^i \rangle \Big]. \quad (6) \end{aligned}$$

$$\begin{aligned}
\langle p_1^f p_2^f p_3^f p_{4c}^f | t_{\pm} \sigma_{\mu} | p_1^i p_2^i p_3^i n_{1c}^i \rangle = & -\delta(p_2^f, p_1^i) \delta(p_3^f, p_2^i) \delta(p_4^f, p_3^i) \langle p_{1c}^f | t_{\pm} \sigma_{\mu} | n_{1c}^i \rangle \\
& + \delta(p_1^f, p_1^i) \delta(p_3^f, p_2^i) \delta(p_4^f, p_3^i) \langle p_{2c}^f | t_{\pm} \sigma_{\mu} | n_{1c}^i \rangle \\
& - \delta(p_1^f, p_1^i) \delta(p_2^f, p_2^i) \delta(p_4^f, p_3^i) \langle p_{3c}^f | t_{\pm} \sigma_{\mu} | n_{1c}^i \rangle \\
& + \delta(p_1^f, p_1^i) \delta(p_2^f, p_2^i) \delta(p_3^f, p_3^i) \langle p_{4c}^f | t_{\pm} \sigma_{\mu} | n_{1c}^i \rangle. \quad (7)
\end{aligned}$$

$$\begin{aligned}
\langle p_1^f p_2^f n_1^f n_{2c}^f | t_{\pm} \sigma_{\mu} | p_1^i n_1^i n_2^i n_{3c}^i \rangle = & \delta(p_1^f, p_1^i) \left[\delta(n_1^f, n_2^i) \delta(n_2^f, n_3^i) \langle p_{2c}^f | t_{\pm} \sigma_{\mu} | n_{1c}^i \rangle \right. \\
& - \delta(n_1^f, n_1^i) \delta(n_2^f, n_3^i) \langle p_{2c}^f | t_{\pm} \sigma_{\mu} | n_{2c}^i \rangle \\
& + \delta(n_1^f, n_1^i) \delta(n_2^f, n_2^i) \langle p_{2c}^f | t_{\pm} \sigma_{\mu} | n_{3c}^i \rangle \Big] \\
& - \delta(p_2^f, p_1^i) \left[\delta(n_1^f, n_2^i) \delta(n_2^f, n_3^i) \langle p_{1c}^f | t_{\pm} \sigma_{\mu} | n_{1c}^i \rangle \right. \\
& - \delta(n_1^f, n_1^i) \delta(n_2^f, n_3^i) \langle p_{1c}^f | t_{\pm} \sigma_{\mu} | n_{2c}^i \rangle \\
& + \delta(n_1^f, n_1^i) \delta(n_2^f, n_2^i) \langle p_{1c}^f | t_{\pm} \sigma_{\mu} | n_{3c}^i \rangle \Big]. \quad (8)
\end{aligned}$$

$$\begin{aligned}
\langle n_1^f n_2^f n_3^f n_{4c}^f | t_{\pm} \sigma_{-\mu} | p_1^i n_1^i n_2^i n_{3c}^i \rangle = & \delta(n_2^f, n_1^i) \delta(n_3^f, n_2^i) \delta(n_4^f, n_3^i) \langle n_{1c}^f | t_{\pm} \sigma_{-\mu} | p_{1c}^i \rangle \\
& - \delta(n_1^f, n_1^i) \delta(n_3^f, n_2^i) \delta(n_4^f, n_3^i) \langle n_{2c}^f | t_{\pm} \sigma_{-\mu} | p_{1c}^i \rangle \\
& + \delta(n_1^f, n_1^i) \delta(n_2^f, n_2^i) \delta(n_4^f, n_3^i) \langle n_{3c}^f | t_{\pm} \sigma_{-\mu} | p_{1c}^i \rangle \\
& - \delta(n_1^f, n_1^i) \delta(n_2^f, n_2^i) \delta(n_3^f, n_3^i) \langle n_{4c}^f | t_{\pm} \sigma_{-\mu} | p_{1c}^i \rangle. \quad (9)
\end{aligned}$$

For all quasiparticle transition amplitudes (Eqns. (2)-(9)), we took into account the antisymmetrization of the single-quasiparticle states

$$\begin{aligned}
p_1^f &< p_2^f < p_3^f < p_4^f \\
n_1^f &< n_2^f < n_3^f < n_4^f \\
p_1^i &< p_2^i < p_3^i < p_4^i \\
n_1^i &< n_2^i < n_3^i < n_4^i
\end{aligned}$$

GT transitions of phonon excitations for every excited state were also taken into account. We also assumed that the quasiparticles in the parent nucleus remained in the same quasiparticle orbits.

In order to further increase the reliability of our calculations, we did incorporate experimental data wherever applicable. The calculated excitation energies (along with their *log ft* values, if available) were replaced with the measured one when they were within 0.5 MeV of each other. Missing measured states were inserted. However, we did not replace (insert) theoretical levels with the experimental ones beyond the level in experimental compilations without definite spin and/or parity assignment.

3. Results and Discussion

^{56}Ni is a doubly magic nucleus which is believed to be copiously produced in the supernova conditions and is considered to be a prime candidate for electron capturing. In this work we considered 30 states (up to excitation energy of 10 MeV) in ^{56}Ni . States higher in energy have a negligible probability of occupation for the temperature and density scales chosen for this phase of collapse. Table 1 lists the calculated parent excited states of ^{56}Ni in order of increasing energy. We start by presenting the GT strength distribution functions for the ground and first two excited states of ^{56}Ni . Complete set of GT strength distribution functions for higher excited states can be requested by email to the corresponding author. We considered around 200 states of daughters, ^{56}Co and ^{56}Cu , for electron and positron captures, respectively, up to excitation energy around 45 MeV. GT transitions are dominant excitation mode for the electron and positron captures during the presupernova evolution. The energy dependence of weak interaction matrix elements (or equivalently, the GT strength distributions) is unknown for many nuclei of potential importance in presupernova stars and collapsing cores. The centroid of the GT distribution determines the effective energy of electron capture from the ground state of the parent nucleus to the excited state of the daughter nucleus. This along with the electron-Fermi energy determines which nuclei are able to capture electron from, or β -decay onto the Fermi-sea at a given temperature and density and thus control the rate at which the abundance of a particular nuclei would change in the presupernova core. The GT strength distributions for the electron captures and positron captures are shown in Figs. 1 and 2, respectively. Table 2a states the $B(\text{GT}_+)$ strength values for the ground state of ^{56}Ni whereas Table 2b gives the $B(\text{GT}_-)$ strength values. The strengths are given up to energy of 10 MeV in daughter nuclei. Calculated GT strength of magnitude less than 10^{-3} are not included in this table. (In the online version of this paper we replace Table 2 by Table 4 which also contains the GT strength distribution functions for the first and second excited states of ^{56}Ni in both directions.) For the calculation of the associated electron captures on ^{56}Ni , the authors in [23] calculated the $B(\text{GT}_+)$ strength only from the ground state. Our calculations of electron capture rates include contributions from the ground as well as the 30 excited states given in Table 1. Our calculations show that for the ground state of ^{56}Ni the centroid of the GT_+ strength resides at energy around 5.7 MeV in daughter ^{56}Co (see also [15]). FFN [12] placed the GT_+ resonance in ^{56}Co at energy 3.8 MeV. The GT_+ centroid of [23] is at energy around 2.5-3.0 MeV in daughter ^{56}Co . The GT_+ centroids for the first and second excited states of ^{56}Ni are around 7.9 MeV and 11.4 MeV in daughter ^{56}Co , respectively. For the ground state of ^{56}Ni , we calculated total GT_+ strength of 8.9 as compared to the values 10.1 and 9.8 ± 4 calculated by [23] and shell model Monte Carlo calculations (SMMC) [24], respectively.

Analyzing $B(\text{GT}_-)$ strength (Fig. 2), we note that our ground state GT centroid resides at energy around 4.7 MeV in daughter, ^{56}Cu . For positron captures, we calculated the total GT_- strength for the ground state of 7.4 for ^{56}Ni while authors in [25] calculated it to be 11.4 (see their Table 3, experimental values were not mentioned). For the first and second excited states our GT_-

centroid resides around 7.6 MeV and 8.6 MeV in daughter ^{56}Cu , respectively.

Fig. 3 shows the variation with densities and temperatures of our calculated electron capture rates for ^{56}Ni . The temperature scale T_9 measures the temperature in 10^9K and the density in the inset has units of g/cm^3 . It is pertinent to mention that contributions from all excited states are included in the final calculation of these capture rates. We calculated these weak rates for densities in the range $(10^{0.5} - 10^{11})\text{g}/\text{cm}^3$ and for temperature scales $T_9 = 0.5$ to 30. We note that the electron capture rates increase with increasing temperatures and densities. It is also worth mentioning that for low and intermediate densities in the range $(10^{0.5} - 10^8)\text{g}/\text{cm}^3$ the electron capture rates converge to a value of around 500 s^{-1} at $T_9 = 30$. At higher densities order of magnitude differences start to build in between the corresponding rates. The gradient of the curves at low and intermediate temperatures ($T_9 = 0.5$ to 10) also decreases with increasing density. At densities in the vicinity of $10^{11}\text{g}/\text{cm}^3$ the electron capture rates remain constant until the stellar core approaches temperature around $\log T = 10$ K. We observed a similar trend for electron captures on ^{55}Co [26] but the capture rates of this nucleus were slower than electron capture rates on ^{56}Ni . We also noted that capture rates of ^{56}Ni is one order of magnitude faster than that of ^{55}Co when the stellar core shifts from densities $(10^7$ to $10^{11})\text{g}/\text{cm}^3$ at low temperatures (around $\log T = 7.0$).

FFN calculated electron and positron capture rates for nuclei in the range $A = 21$ -60. The GT contribution to the rate was parameterized on the basis of the independent particle model and supplemented by a contribution simulating low-lying transitions. Fig. 4 depicts the comparison of our electron capture rates with the FFN rates [12] for densities $\rho Y_e = 10^3\text{g}/\text{cm}^3$ and $\rho Y_e = 10^{11}\text{g}/\text{cm}^3$. At low densities (around $\rho Y_e = 10^3\text{g}/\text{cm}^3$) and temperatures (around $\log T = 9.0$), our electron capture rates for ^{56}Ni are in good agreement with FFN capture rates. As the temperature of the stellar core increases the FFN gradients becomes steeper. At temperatures $\log T > 9.5$, we note that the FFN rates are enhanced than our rates. At high temperatures the probability of occupation of the parent excited states (E_i) increases, FFN did not take into effect the process of particle emission from excited states (this process is accounted for in the present pn-QRPA calculations). FFN's parent excitation energies (E_i) are well above the particle decay channel and partly contribute to the enhancement of their electron capture rates at higher temperatures.

We also compared our calculation of electron capture rates with those calculated using large-scale shell model [23]. Fig. 6 in Ref. [15] compares the two calculations. In order to save space, we decided not to discuss the comparison in this paper. The core-collapse simulators should take note of our enhanced electron capture rates compared to shell model results at *presupernova temperatures*. (For details we refer to [15].)

One of the channels for the energy release from the star is the neutrino emission which is mainly from the e/e^+ capture on nucleons and e^\pm annihilation. Positron capture plays a crucial role in the dynamics of stellar core. They play an indirect role in the reduction of degeneracy pressure of the electrons in the core. Fig. 5 shows our positron capture rates on ^{56}Ni . We note that the

positron capture rates are very slow as compared to electron capture on ^{56}Ni . The positron capture rates enhance as temperature of the stellar core increases. We also observe that the positron capture rates are almost the same for the densities in the range $(10 - 10^6)\text{g/cm}^3$. When the densities increase beyond this range a decline in the positron capture rate starts. At temperature $\log T = 10.5$, when the stellar core shifts from density $(10^7 \text{ to } 10^{11})\text{g/cm}^3$, we observe a decline of 3 orders of magnitude in the positron capture rates.

4. Summary

We have performed pn-QRPA calculations to determine the presupernova electron and positron capture rates on ^{56}Ni for selected densities and temperatures from astrophysical point of view. ^{56}Ni is considered to be amongst the most important nuclei for capturing electrons in the presupernova conditions and core collapse phase. We have also presented our calculated rates on a finer temperature-density grid which might prove useful as a test suite for advanced interpolation routines. Though our centroid is at high excitation energies in daughter but still our electron capture rates are enhanced as compared to shell model rates at presupernova temperatures. Core collapse simulators may find it convenient to take note of these enhanced capture rates. One of the main reasons for these enhanced rates is the *microscopic* calculation of GT strength from the excited states. The pn-QRPA gave us the liberty of using a large model space of $7\hbar\omega$ and proved to be a judicious choice for handling excited states in heavy nuclei in the stellar environment. Table 3 shows our calculations of electron and positron capture rates on ^{56}Ni on a fine grid of temperature-density scale. (In the online version of this paper Table 3 is replaced by Table 5 which also contains the (anti)neutrino energy loss rates.)

Aufderheide et al. [14] reported that the rate of change of lepton-to-baryon ratio ($\dot{\Psi}$) in the stellar core changes by about 25% alone due to the electron captures on ^{56}Ni . Due to our enhanced electron capture rates in the presupernova epoch, the core should radiate out more energy by the process of neutrino emission, keeping the core on a trajectory with lower temperature and entropy. It is also to be noted that Hix and collaborators [3] were unable to find an explosion of their spherically symmetric core collapse simulations. One main reason pointed out by the authors for this failure was the relatively suppressed electron capture rates used in their simulations. It might be interesting to find if our reported rates are in favor of a (prompt) explosion.

This work is partially supported by the ICTP (Italy) through the OEA-project-Prj-16.

References

- [1] D. A. Ostlie, B. W. Carrol, *An Introduction to Modern Stellar Astrophysics*, (Addison-Wisley Publishing Company, Inc., 1996).
- [2] B. E. J. Pagel, *Nucleosynthesis and Chemical Evolution of Galaxies*, (Cambridge Uni. Press, 1997).
- [3] W. R. Hix, O. E. B. Messer, A. Mezzacappa, M. Liebendrfer, J. Sampaio, K. Langanke, D. J. Dean, G. Martinez-Pinedo, *Phys. Rev. Lett.* **91**, 201102 (2003).
- [4] H. A. Bethe, G. E. Brown, J. Applegate, J. Lattimer, *Nucl. Phys. A* **234**, 487 (1979).
- [5] F. K. Sutaria, A. Ray, J. A. Sheikh, P. Ring, *Astron. Astrophys.* **349**, 135 (1999).
- [6] J.-U. Nabi, PhD Thesis, Heidelberg University, Germany, 1999.
- [7] J.-U. Nabi, H. V. Klapdor-Kliengrothaus, *Atomic Data and Nuclear Data Tables* **71**, 149 (1999).
- [8] J.-U. Nabi, H. V. Klapdor-Kliengrothaus, *Atomic Data and Nuclear Data Tables* **88**, 237 (2004).
- [9] J.-U. Nabi, M.-U. Rahman, *Phys. Rev. C* **75**, 035803 (2007).
- [10] J.-U. Nabi, M. Sajjad, accepted for publication in *Phys. Rev. C* (2007).
- [11] J.-U. Nabi, M. Sajjad, M.-U. Rahman, *Acta. Phys. Polon. B* **38**, 3203 (2007).
- [12] G. M. Fuller, W. A. Fowler, M. J. Newman, *ApJS* **42**, 447 (1980); **48**, 279 (1982); *ApJ* **252**, 715 (1982).
- [13] M. B. Aufderheide, G. E. Brwon, T. T. S. Kuo, D. B. Stout, P. Vogel, *Astrophys. J.* **362**, 241 (1990).
- [14] M. B. Aufderheide, I. Fushiki, S. E. Woosley, D. H. Hartman, *Astrophys. J. Suppl.* **91**, 389 (1994).
- [15] J.-U. Nabi, M.-U. Rahman, *Phys. Lett. B* **612**, 190 (2005).
- [16] S. G. Nilsson, *Mat. Fys. Medd. Dan. Vid. Selsk* **29** 16 (1955).
- [17] A. Staudt, E. Bender, K. Muto, H. V. Klapdor-Kleingrothaus, *Atomic Data and Nuclear Data Tables* **44**, 79 (1990).
- [18] M. Hirsch, A. Staudt, K. Muto, H. V. Klapdor-Kleingrothaus, *Atomic Data and Nuclear Data Tables* **53**, 165 (1993).

- [19] I. Ragnarsson, R. K. Sheline, *Phys. Scr.* **29**, 385 (1984).
- [20] M. Hirsch, A. Staudt, K. Muto, H. V. Klapdor-Kliengrothaus, *Nucl. Phys. A* **535**, 62 (1991).
- [21] G. Audi, A. H. Wapstra, and C. Thibault, *Nucl. Phys. A* **729**, 337 (2003).
- [22] K. Grotz, H. V. Klapdor, The Weak Interaction in Nuclear, Particle and Astrophysics, Adam Hilger, (IOP Publishing, Bristol, Philadelphia, New York, 1990).
- [23] K. Langanke, G. Martinez-Pinedo, *Phys. Lett. B* **436**, 19 (1998).
- [24] K. Langanke, D. J. Dean, P. B. Radha, Y. Alhassid, S. E. Koonin, *Phys. Rev. C* **52**, 718 (1995).
- [25] H. Nakada, T. Sebe, *J. Phys. G* **22**, 1349 (1996).
- [26] J.-U. Nabi, M.-U. Rahman, M. Sajjad, accepted for publication in *Braz. J. Phys.*, **37** (2007).

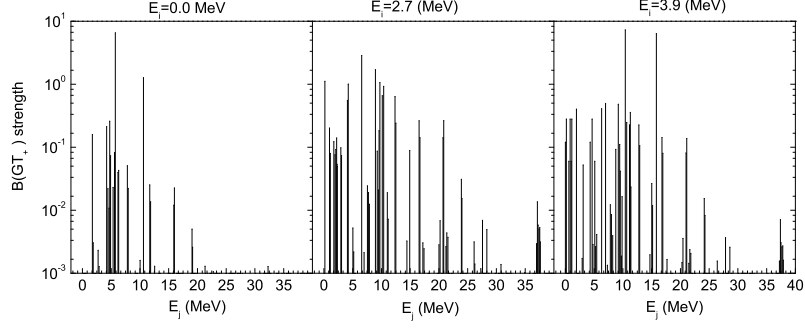


Figure 1: Gamow-Teller (GT_+) strength distributions for ^{56}Ni . From left to right, the panels show the GT_+ strength for ground, 1^{st} , and 2^{nd} excited states, respectively. E_i (E_j) represents energy of parent (daughter) states. The energy scale refers to the excitation energies in the daughter ^{56}Co .

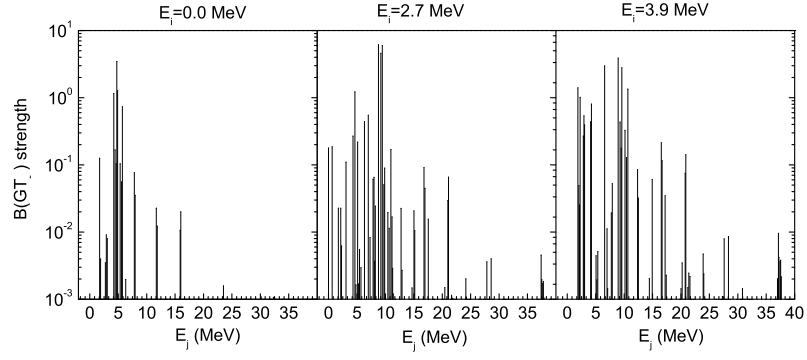


Figure 2: Gamow-Teller (GT_-) strength distributions for ^{56}Ni . From left to right, the panels show GT_- strength for ground, 1^{st} , and 2^{nd} excited states, respectively. E_i (E_j) represents energy of parent (daughter) states. The energy scale refers to excitation energies in the daughter ^{56}Cu .

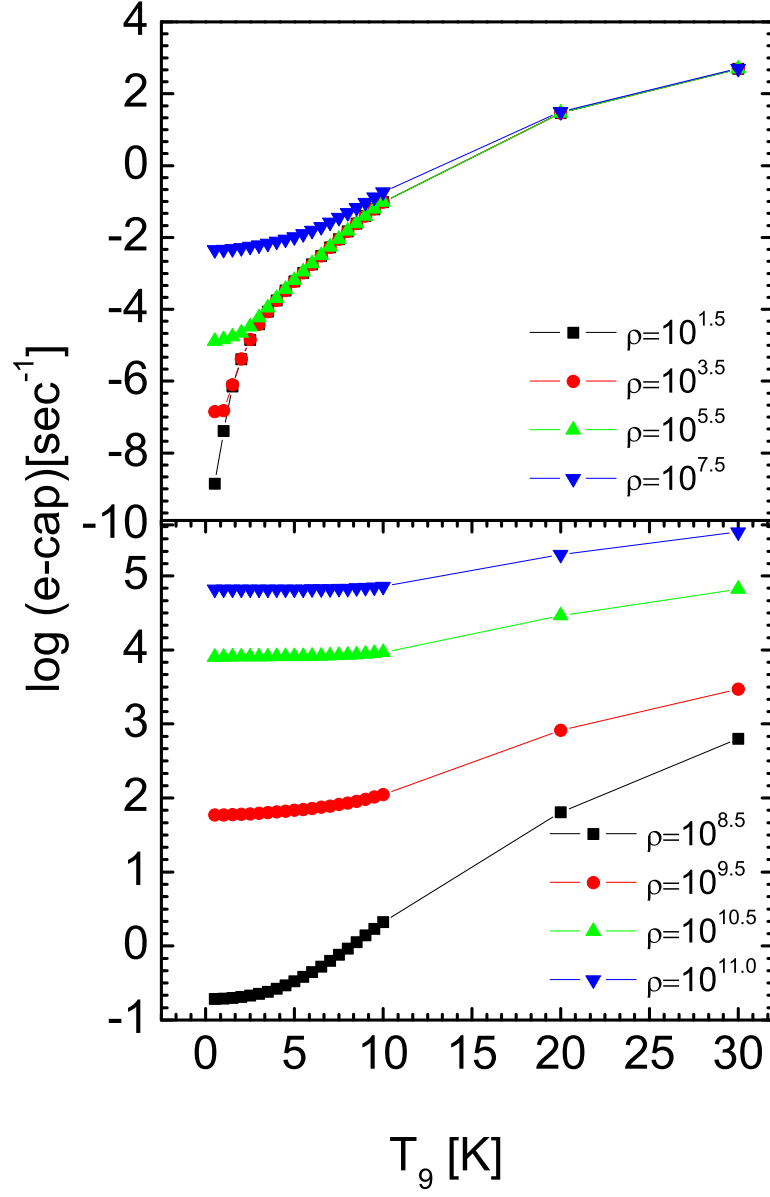


Figure 3: Calculated electron captures rates (in logarithmic scale) on ^{56}Ni as function of temperatures for different selected densities. The densities in the legend are in units of g/cm^3 whereas T_9 represents temperature in units of $10^9 K$.

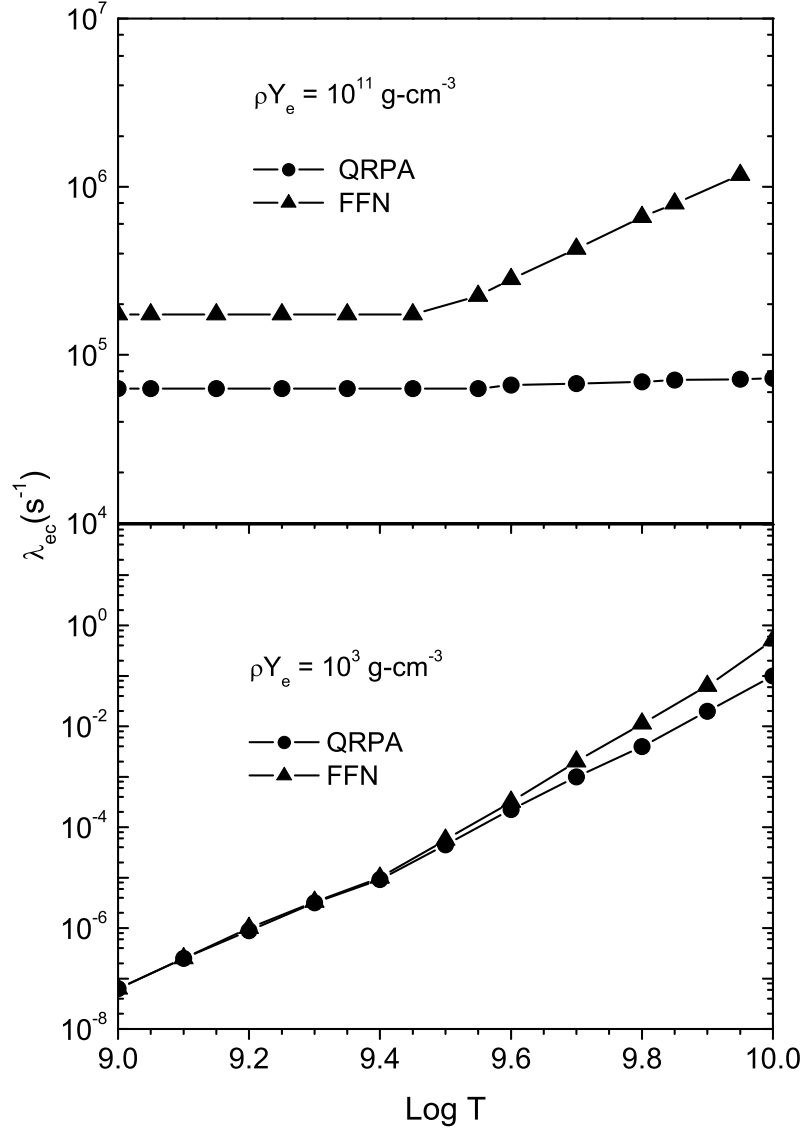


Figure 4: Comparison of QRPA electron capture rates with those of FFN [12] on ^{56}Ni as function of temperature. The upper panel is for density 10^{11} g/cm^3 while the lower panel is for density 10^3 g/cm^3 .

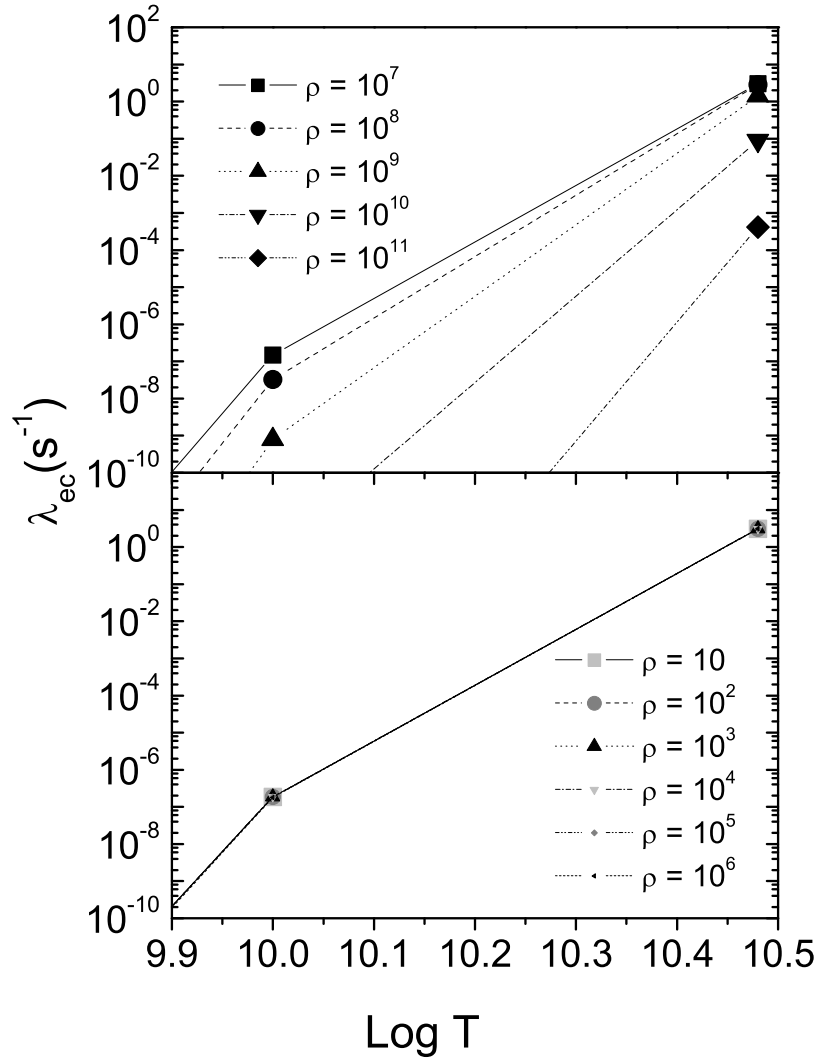


Figure 5: Positron captures rates on ^{56}Ni as function of temperatures for different selected densities. The densities in the legend are in units of g/cm^3 .

Table 1: Calculated excited states in parent ^{56}Ni .

0.00	5.23	6.01	7.29	7.76	8.80
2.70	5.39	6.21	7.35	7.86	9.12
3.96	5.47	6.32	7.48	8.08	9.29
4.97	5.68	6.44	7.53	8.31	9.71
5.08	5.76	6.65	7.62	8.56	9.98

Table 2a: Calculated B(GT+) values from ground state in ^{56}Ni .

Energy(MeV)	B(GT+)	Energy(MeV)	B(GT+)	Energy(MeV)	B(GT+)
1.72	1.59E-01	4.63	1.08E-02	6.18	3.98E-02
1.88	3.03E-03	4.74	2.59E-01	6.31	4.31E-02
2.72	2.32E-03	4.88	7.32E-02	7.82	5.10E-02
2.90	1.28E-03	5.33	2.30E-02	7.97	2.22E-02
4.21	2.12E-01	5.56	8.27E-02	10.03	1.60E-03
4.44	2.20E-02	5.73	6.54E+00		

Table 2b: Calculated B(GT-) values from ground state in ^{56}Ni .

Energy(MeV)	B(GT-)	Energy(MeV)	B(GT-)	Energy(MeV)	B(GT-)
1.72	1.26E-01	4.44	1.67E-01	5.73	7.32E-01
1.88	3.98E-03	4.63	1.03E-01	6.31	1.97E-03
2.72	3.50E-03	4.74	3.48E+00	7.82	7.67E-02
2.90	9.08E-03	4.88	1.27E+00	7.97	3.52E-02
3.08	8.00E-03	5.33	1.04E-01		
4.21	1.15E+00	5.56	5.59E-02		

Table 3: Calculated electron and positron capture rates on ^{56}Ni for different selected densities and temperatures in stellar matter. Aden is $\log(\rho Y_e)$ and has units of g/cm^3 , where ρ is the baryon density and Y_e is the ratio of the electron number to the baryon number. Temperatures (T_9) are measured in $10^9 K$. E-cap and E+cap are the electron and positron capture rates, respectively. The calculated electron and positron capture rates are tabulated in logarithmic (to base 10) scale in units of sec^{-1} . In the table, -100.000 means that the rate is smaller than 10^{-100} .

Aden	T_9	E-cap	E+cap	Aden	T_9	E-cap	E+cap
0.5	0.50	-9.828	-100.000	1.5	0.50	-8.850	-100.000
0.5	1.00	-7.394	-81.298	1.5	1.00	-7.387	-81.305
0.5	1.50	-6.148	-54.201	1.5	1.50	-6.147	-54.201
0.5	2.00	-5.391	-40.556	1.5	2.00	-5.391	-40.556
0.5	2.50	-4.846	-32.317	1.5	2.50	-4.846	-32.317
0.5	3.00	-4.418	-26.790	1.5	3.00	-4.418	-26.790
0.5	3.50	-4.063	-22.817	1.5	3.50	-4.062	-22.817
0.5	4.00	-3.756	-19.818	1.5	4.00	-3.755	-19.817
0.5	4.50	-3.481	-17.468	1.5	4.50	-3.481	-17.468
0.5	5.00	-3.227	-15.575	1.5	5.00	-3.226	-15.575
0.5	5.50	-2.984	-14.014	1.5	5.50	-2.983	-14.013
0.5	6.00	-2.747	-12.702	1.5	6.00	-2.746	-12.702
0.5	6.50	-2.512	-11.583	1.5	6.50	-2.512	-11.583
0.5	7.00	-2.281	-10.615	1.5	7.00	-2.280	-10.615
0.5	7.50	-2.053	-9.769	1.5	7.50	-2.053	-9.768
0.5	8.00	-1.831	-9.021	1.5	8.00	-1.831	-9.020
0.5	8.50	-1.616	-8.354	1.5	8.50	-1.616	-8.354
0.5	9.00	-1.410	-7.756	1.5	9.00	-1.409	-7.755
0.5	9.50	-1.211	-7.215	1.5	9.50	-1.211	-7.215
0.5	10.00	-1.022	-6.724	1.5	10.00	-1.021	-6.723
0.5	20.00	1.464	-1.625	1.5	20.00	1.465	-1.623
0.5	30.00	2.691	0.473	1.5	30.00	2.693	0.474
1.0	0.50	-9.348	-100.000	2.0	0.50	-8.350	-100.000
1.0	1.00	-7.392	-81.300	2.0	1.00	-7.370	-81.321
1.0	1.50	-6.148	-54.200	2.0	1.50	-6.146	-54.202
1.0	2.00	-5.391	-40.556	2.0	2.00	-5.390	-40.556
1.0	2.50	-4.846	-32.317	2.0	2.50	-4.846	-32.317
1.0	3.00	-4.418	-26.790	2.0	3.00	-4.418	-26.790
1.0	3.50	-4.062	-22.817	2.0	3.50	-4.062	-22.817
1.0	4.00	-3.755	-19.817	2.0	4.00	-3.755	-19.817
1.0	4.50	-3.481	-17.468	2.0	4.50	-3.480	-17.468
1.0	5.00	-3.226	-15.575	2.0	5.00	-3.226	-15.575
1.0	5.50	-2.983	-14.014	2.0	5.50	-2.983	-14.013
1.0	6.00	-2.746	-12.702	2.0	6.00	-2.746	-12.702
1.0	6.50	-2.512	-11.583	2.0	6.50	-2.512	-11.583
1.0	7.00	-2.280	-10.615	2.0	7.00	-2.280	-10.615
1.0	7.50	-2.053	-9.768	2.0	7.50	-2.053	-9.768
1.0	8.00	-1.831	-9.020	2.0	8.00	-1.831	-9.020
1.0	8.50	-1.616	-8.354	2.0	8.50	-1.616	-8.354
1.0	9.00	-1.409	-7.756	2.0	9.00	-1.409	-7.755
1.0	9.50	-1.211	-7.215	2.0	9.50	-1.211	-7.215
1.0	10.00	-1.021	-6.723	2.0	10.00	-1.021	-6.723
1.0	20.00	1.465	-1.624	2.0	20.00	1.465	-1.623
1.0	30.00	2.692	0.474	2.0	30.00	2.693	0.474

Aden	T_9	E-cap	E+cap	Aden	T_9	E-cap	E+cap
2.5	0.50	-7.850	-100.000	3.5	0.50	-6.851	-100.000
2.5	1.00	-7.319	-81.373	3.5	1.00	-6.818	-81.875
2.5	1.50	-6.143	-54.205	3.5	1.50	-6.097	-54.251
2.5	2.00	-5.390	-40.557	3.5	2.00	-5.380	-40.567
2.5	2.50	-4.846	-32.317	3.5	2.50	-4.842	-32.321
2.5	3.00	-4.418	-26.790	3.5	3.00	-4.416	-26.791
2.5	3.50	-4.062	-22.817	3.5	3.50	-4.061	-22.818
2.5	4.00	-3.755	-19.817	3.5	4.00	-3.755	-19.818
2.5	4.50	-3.480	-17.468	3.5	4.50	-3.480	-17.468
2.5	5.00	-3.226	-15.575	3.5	5.00	-3.226	-15.575
2.5	5.50	-2.983	-14.013	3.5	5.50	-2.983	-14.014
2.5	6.00	-2.746	-12.702	3.5	6.00	-2.746	-12.702
2.5	6.50	-2.512	-11.583	3.5	6.50	-2.512	-11.583
2.5	7.00	-2.280	-10.615	3.5	7.00	-2.280	-10.615
2.5	7.50	-2.053	-9.768	3.5	7.50	-2.053	-9.768
2.5	8.00	-1.831	-9.020	3.5	8.00	-1.831	-9.020
2.5	8.50	-1.616	-8.354	3.5	8.50	-1.616	-8.354
2.5	9.00	-1.409	-7.755	3.5	9.00	-1.409	-7.755
2.5	9.50	-1.210	-7.215	3.5	9.50	-1.210	-7.215
2.5	10.00	-1.021	-6.723	3.5	10.00	-1.021	-6.723
2.5	20.00	1.465	-1.623	3.5	20.00	1.465	-1.623
2.5	30.00	2.693	0.475	3.5	30.00	2.693	0.475
3.0	0.50	-7.350	-100.000	4.0	0.50	-6.353	-100.000
3.0	1.00	-7.165	-81.527	4.0	1.00	-6.346	-82.350
3.0	1.50	-6.132	-54.216	4.0	1.50	-5.991	-54.358
3.0	2.00	-5.387	-40.559	4.0	2.00	-5.356	-40.591
3.0	2.50	-4.845	-32.318	4.0	2.50	-4.834	-32.329
3.0	3.00	-4.417	-26.790	4.0	3.00	-4.412	-26.796
3.0	3.50	-4.062	-22.817	4.0	3.50	-4.059	-22.820
3.0	4.00	-3.755	-19.817	4.0	4.00	-3.753	-19.819
3.0	4.50	-3.480	-17.468	4.0	4.50	-3.479	-17.469
3.0	5.00	-3.226	-15.575	4.0	5.00	-3.225	-15.575
3.0	5.50	-2.983	-14.013	4.0	5.50	-2.982	-14.014
3.0	6.00	-2.746	-12.702	4.0	6.00	-2.745	-12.702
3.0	6.50	-2.512	-11.583	4.0	6.50	-2.511	-11.583
3.0	7.00	-2.280	-10.615	4.0	7.00	-2.280	-10.615
3.0	7.50	-2.053	-9.768	4.0	7.50	-2.052	-9.768
3.0	8.00	-1.831	-9.020	4.0	8.00	-1.830	-9.020
3.0	8.50	-1.616	-8.354	4.0	8.50	-1.616	-8.354
3.0	9.00	-1.409	-7.755	4.0	9.00	-1.409	-7.755
3.0	9.50	-1.210	-7.214	4.0	9.50	-1.210	-7.215
3.0	10.00	-1.021	-6.723	4.0	10.00	-1.021	-6.723
3.0	20.00	1.465	-1.623	4.0	20.00	1.465	-1.623
3.0	30.00	2.693	0.475	4.0	30.00	2.693	0.475

Aden	T_9	E-cap	E+cap	Aden	T_9	E-cap	E+cap
4.5	0.50	-5.858	-100.000	5.5	0.50	-4.889	-100.000
4.5	1.00	-5.849	-82.855	5.5	1.00	-4.845	-83.961
4.5	1.50	-5.715	-54.636	5.5	1.50	-4.768	-55.622
4.5	2.00	-5.282	-40.666	5.5	2.00	-4.663	-41.300
4.5	2.50	-4.807	-32.357	5.5	2.50	-4.490	-32.680
4.5	3.00	-4.399	-26.808	5.5	3.00	-4.237	-26.974
4.5	3.50	-4.052	-22.827	5.5	3.50	-3.961	-22.920
4.5	4.00	-3.749	-19.823	5.5	4.00	-3.693	-19.881
4.5	4.50	-3.476	-17.472	5.5	4.50	-3.439	-17.510
4.5	5.00	-3.223	-15.577	5.5	5.00	-3.197	-15.604
4.5	5.50	-2.981	-14.015	5.5	5.50	-2.962	-14.035
4.5	6.00	-2.744	-12.703	5.5	6.00	-2.730	-12.718
4.5	6.50	-2.511	-11.584	5.5	6.50	-2.500	-11.595
4.5	7.00	-2.279	-10.615	5.5	7.00	-2.271	-10.624
4.5	7.50	-2.052	-9.769	5.5	7.50	-2.045	-9.776
4.5	8.00	-1.830	-9.021	5.5	8.00	-1.824	-9.026
4.5	8.50	-1.615	-8.354	5.5	8.50	-1.611	-8.359
4.5	9.00	-1.408	-7.756	5.5	9.00	-1.405	-7.760
4.5	9.50	-1.210	-7.215	5.5	9.50	-1.207	-7.218
4.5	10.00	-1.020	-6.723	5.5	10.00	-1.018	-6.726
4.5	20.00	1.465	-1.623	5.5	20.00	1.466	-1.624
4.5	30.00	2.693	0.475	5.5	30.00	2.693	0.475
5.0	0.50	-5.372	-100.000	6.0	0.50	-4.377	-100.000
5.0	1.00	-5.348	-83.381	6.0	1.00	-4.321	-84.685
5.0	1.50	-5.269	-55.092	6.0	1.50	-4.246	-56.229
5.0	2.00	-5.071	-40.879	6.0	2.00	-4.158	-41.847
5.0	2.50	-4.723	-32.442	6.0	2.50	-4.058	-33.133
5.0	3.00	-4.359	-26.849	6.0	3.00	-3.930	-27.292
5.0	3.50	-4.030	-22.849	6.0	3.50	-3.762	-23.125
5.0	4.00	-3.735	-19.837	6.0	4.00	-3.564	-20.014
5.0	4.50	-3.467	-17.481	6.0	4.50	-3.352	-17.599
5.0	5.00	-3.217	-15.584	6.0	5.00	-3.136	-15.667
5.0	5.50	-2.977	-14.020	6.0	5.50	-2.918	-14.080
5.0	6.00	-2.741	-12.707	6.0	6.00	-2.697	-12.752
5.0	6.50	-2.508	-11.586	6.0	6.50	-2.474	-11.621
5.0	7.00	-2.277	-10.618	6.0	7.00	-2.250	-10.645
5.0	7.50	-2.050	-9.770	6.0	7.50	-2.029	-9.792
5.0	8.00	-1.829	-9.022	6.0	8.00	-1.811	-9.040
5.0	8.50	-1.614	-8.355	6.0	8.50	-1.600	-8.370
5.0	9.00	-1.407	-7.757	6.0	9.00	-1.395	-7.769
5.0	9.50	-1.209	-7.216	6.0	9.50	-1.199	-7.226
5.0	10.00	-1.020	-6.724	6.0	10.00	-1.011	-6.733
5.0	20.00	1.465	-1.623	6.0	20.00	1.467	-1.624
5.0	30.00	2.693	0.475	6.0	30.00	2.693	0.474

Aden	T_9	E-cap	E+cap	Aden	T_9	E-cap	E+cap
6.5	0.50	-3.785	-100.000	7.5	0.50	-2.345	-100.000
6.5	1.00	-3.741	-85.731	7.5	1.00	-2.332	-89.832
6.5	1.50	-3.678	-57.012	7.5	1.50	-2.310	-59.827
6.5	2.00	-3.605	-42.513	7.5	2.00	-2.281	-44.709
6.5	2.50	-3.526	-33.729	7.5	2.50	-2.245	-35.571
6.5	3.00	-3.442	-27.818	7.5	3.00	-2.205	-29.432
6.5	3.50	-3.349	-23.561	7.5	3.50	-2.159	-25.011
6.5	4.00	-3.240	-20.351	7.5	4.00	-2.108	-21.667
6.5	4.50	-3.109	-17.851	7.5	4.50	-2.049	-19.042
6.5	5.00	-2.955	-15.854	7.5	5.00	-1.980	-16.921
6.5	5.50	-2.781	-14.220	7.5	5.50	-1.899	-15.169
6.5	6.00	-2.593	-12.859	7.5	6.00	-1.804	-13.695
6.5	6.50	-2.393	-11.704	7.5	6.50	-1.696	-12.436
6.5	7.00	-2.186	-10.711	7.5	7.00	-1.576	-11.348
6.5	7.50	-1.977	-9.845	7.5	7.50	-1.446	-10.397
6.5	8.00	-1.769	-9.083	7.5	8.00	-1.309	-9.560
6.5	8.50	-1.565	-8.406	7.5	8.50	-1.167	-8.818
6.5	9.00	-1.366	-7.799	7.5	9.00	-1.022	-8.155
6.5	9.50	-1.175	-7.251	7.5	9.50	-0.876	-7.560
6.5	10.00	-0.990	-6.754	7.5	10.00	-0.731	-7.022
6.5	20.00	1.469	-1.627	7.5	20.00	1.502	-1.661
6.5	30.00	2.694	0.474	7.5	30.00	2.704	0.464
7.0	0.50	-3.101	-100.000	8.0	0.50	-1.550	-100.000
7.0	1.00	-3.074	-87.347	8.0	1.00	-1.543	-93.578
7.0	1.50	-3.034	-58.140	8.0	1.50	-1.532	-62.344
7.0	2.00	-2.983	-43.412	8.0	2.00	-1.516	-46.619
7.0	2.50	-2.925	-34.499	8.0	2.50	-1.496	-37.121
7.0	3.00	-2.863	-28.506	8.0	3.00	-1.471	-30.746
7.0	3.50	-2.797	-24.185	8.0	3.50	-1.440	-26.160
7.0	4.00	-2.726	-20.914	8.0	4.00	-1.402	-22.694
7.0	4.50	-2.646	-18.347	8.0	4.50	-1.355	-19.977
7.0	5.00	-2.552	-16.278	8.0	5.00	-1.298	-17.784
7.0	5.50	-2.442	-14.575	8.0	5.50	-1.231	-15.973
7.0	6.00	-2.311	-13.151	8.0	6.00	-1.152	-14.450
7.0	6.50	-2.162	-11.943	8.0	6.50	-1.063	-13.148
7.0	7.00	-1.997	-10.906	8.0	7.00	-0.966	-12.020
7.0	7.50	-1.821	-10.005	8.0	7.50	-0.861	-11.032
7.0	8.00	-1.640	-9.215	8.0	8.00	-0.752	-10.159
7.0	8.50	-1.457	-8.516	8.0	8.50	-0.641	-9.380
7.0	9.00	-1.276	-7.892	8.0	9.00	-0.528	-8.681
7.0	9.50	-1.098	-7.330	8.0	9.50	-0.415	-8.049
7.0	10.00	-0.925	-6.822	8.0	10.00	-0.302	-7.475
7.0	20.00	1.477	-1.635	8.0	20.00	1.580	-1.742
7.0	30.00	2.696	0.471	8.0	30.00	2.727	0.440

Aden	T_9	E-cap	E+cap	Aden	T_9	E-cap	E+cap
8.5	0.50	-0.714	-100.000	9.5	0.50	1.770	-100.000
8.5	1.00	-0.709	-99.150	9.5	1.00	1.772	-100.000
8.5	1.50	-0.701	-66.073	9.5	1.50	1.776	-79.658
8.5	2.00	-0.689	-49.429	9.5	2.00	1.780	-59.635
8.5	2.50	-0.671	-39.384	9.5	2.50	1.786	-47.565
8.5	3.00	-0.648	-32.647	9.5	3.00	1.793	-39.482
8.5	3.50	-0.617	-27.805	9.5	3.50	1.802	-33.681
8.5	4.00	-0.579	-24.149	9.5	4.00	1.811	-29.308
8.5	4.50	-0.532	-21.285	9.5	4.50	1.822	-25.889
8.5	5.00	-0.478	-18.977	9.5	5.00	1.833	-23.138
8.5	5.50	-0.417	-17.073	9.5	5.50	1.846	-20.874
8.5	6.00	-0.350	-15.473	9.5	6.00	1.860	-18.975
8.5	6.50	-0.278	-14.107	9.5	6.50	1.875	-17.357
8.5	7.00	-0.200	-12.925	9.5	7.00	1.892	-15.961
8.5	7.50	-0.119	-11.891	9.5	7.50	1.911	-14.742
8.5	8.00	-0.034	-10.977	9.5	8.00	1.932	-13.668
8.5	8.50	0.054	-10.162	9.5	8.50	1.956	-12.712
8.5	9.00	0.142	-9.430	9.5	9.00	1.983	-11.856
8.5	9.50	0.232	-8.768	9.5	9.50	2.013	-11.083
8.5	10.00	0.322	-8.166	9.5	10.00	2.046	-10.383
8.5	20.00	1.806	-1.977	9.5	20.00	2.913	-3.212
8.5	30.00	2.800	0.364	9.5	30.00	3.470	-0.341
9.0	0.50	0.385	-100.000	10.0	0.50	2.905	-100.000
9.0	1.00	0.393	-100.000	10.0	1.00	2.906	-100.000
9.0	1.50	0.407	-71.571	10.0	1.50	2.907	-91.541
9.0	2.00	0.425	-53.563	10.0	2.00	2.908	-68.552
9.0	2.50	0.447	-42.701	10.0	2.50	2.910	-54.703
9.0	3.00	0.474	-35.421	10.0	3.00	2.912	-45.435
9.0	3.50	0.504	-30.193	10.0	3.50	2.915	-38.788
9.0	4.00	0.537	-26.249	10.0	4.00	2.918	-33.782
9.0	4.50	0.572	-23.162	10.0	4.50	2.921	-29.870
9.0	5.00	0.610	-20.677	10.0	5.00	2.925	-26.726
9.0	5.50	0.649	-18.629	10.0	5.50	2.929	-24.141
9.0	6.00	0.690	-16.910	10.0	6.00	2.934	-21.975
9.0	6.50	0.734	-15.444	10.0	6.50	2.940	-20.131
9.0	7.00	0.779	-14.177	10.0	7.00	2.946	-18.542
9.0	7.50	0.827	-13.070	10.0	7.50	2.954	-17.156
9.0	8.00	0.878	-12.093	10.0	8.00	2.963	-15.936
9.0	8.50	0.932	-11.222	10.0	8.50	2.974	-14.852
9.0	9.00	0.989	-10.442	10.0	9.00	2.988	-13.882
9.0	9.50	1.048	-9.736	10.0	9.50	3.003	-13.008
9.0	10.00	1.110	-9.096	10.0	10.00	3.021	-12.216
9.0	20.00	2.274	-2.477	10.0	20.00	3.657	-4.204
9.0	30.00	3.014	0.144	10.0	30.00	4.099	-1.064

Aden	T_9	E-cap	E+cap	Aden	T_9	E-cap	E+cap
10.5	0.50	3.905	-100.000	11.0	0.50	4.821	-100.000
10.5	1.00	3.905	-100.000	11.0	1.00	4.821	-100.000
10.5	1.50	3.906	-100.000	11.0	1.50	4.821	-100.000
10.5	2.00	3.906	-81.642	11.0	2.00	4.821	-100.000
10.5	2.50	3.907	-65.179	11.0	2.50	4.821	-80.554
10.5	3.00	3.908	-54.168	11.0	3.00	4.822	-66.983
10.5	3.50	3.909	-46.277	11.0	3.50	4.822	-57.263
10.5	4.00	3.910	-40.338	11.0	4.00	4.822	-49.953
10.5	4.50	3.911	-35.701	11.0	4.50	4.823	-44.251
10.5	5.00	3.912	-31.977	11.0	5.00	4.823	-39.674
10.5	5.50	3.914	-28.918	11.0	5.50	4.824	-35.917
10.5	6.00	3.916	-26.357	11.0	6.00	4.825	-32.775
10.5	6.50	3.918	-24.180	11.0	6.50	4.826	-30.107
10.5	7.00	3.921	-22.305	11.0	7.00	4.828	-27.811
10.5	7.50	3.925	-20.672	11.0	7.50	4.830	-25.813
10.5	8.00	3.930	-19.235	11.0	8.00	4.833	-24.057
10.5	8.50	3.936	-17.960	11.0	8.50	4.838	-22.501
10.5	9.00	3.944	-16.821	11.0	9.00	4.843	-21.112
10.5	9.50	3.954	-15.796	11.0	9.50	4.851	-19.863
10.5	10.00	3.965	-14.868	11.0	10.00	4.860	-18.734
10.5	20.00	4.465	-5.582	11.0	20.00	5.291	-7.552
10.5	30.00	4.821	-2.039	11.0	30.00	5.592	-3.392